nature photonics

Article

https://doi.org/10.1038/s41566-023-01173-5

Mid-gap trap state-mediated dark current in organic photodiodes

Received: 28 January 2022

Accepted: 13 February 2023

Published online: 23 March 2023

Check for updates

Oskar J. Sandberg[1] ✉, Christina Kaiser[1], Stefan Zeiske[1], Nasim Zarrabi[1], Sam Gielen[2,3], Wouter Maes[2,3], Koen Vandewal[2,3], Paul Meredith[1] & Ardalan Armin[1] ✉

Photodiodes are ubiquitous in industry and consumer electronics. Constantly emerging new applications for photodiodes demand different mechanical and optoelectronic properties from those provided by conventional inorganic-based semiconductor devices. This has stimulated considerable interest in the use of organic semiconductors, which provide a vast palette of available optoelectronic properties, can be incorporated into flexible form factor geometries, and promise low-cost, low-embodied energy manufacturing from earth-abundant materials. The sensitivity of a photodiode depends critically on the dark current. Organic photodiodes (OPDs), however, are characterized by a much higher dark current than expected for thermally excited radiative transitions. Here we show that the dark saturation current in OPDs is fundamentally limited by mid-gap trap states. This new insight is generated by the universal trend observed for the dark saturation current of a large set of OPDs and further substantiated by sensitive external-quantum-efficiency- and temperature-dependent current measurements. Based on this insight, an upper limit for the specific detectivity is established. A detailed understanding of the origins of noise in any detector is fundamental to defining performance limitations and thus is critical to materials and device selection, and design and optimization for all applications. Our work establishes these important principles for OPDs.

Organic semiconductors present promising complementary alternatives to inorganic semiconductors for photodetection, in particular in the wavelength (λ) range between 1 and 2 µm (ref. [1]). This spectral window is interesting for bioimaging[2], optical telecommunication[3] and machine vision[4]. The advantages of organic semiconductors include monolithic integrability with silicon readout circuitry[5,6], reduced material and manufacturing costs from earth-abundant feedstocks, and inherent material properties like flexibility, bandgap tunability and light weight[7]. Combining these properties with state-of-the-art device performance and operational lifetimes is expected to result in disruptive innovations, particularly in the field of consumer electronics[8], such as previously demonstrated with organic light-emitting diodes.

In the past decade, advances in absorber materials and device architectures used in organic photodiodes (OPDs) based on donor (D):acceptor (A) bulk heterojunction (BHJ) semiconductor blends have delivered substantial performance improvements. The key quality metric of a photodetector is the specific detectivity:

$$D^* = \frac{q\lambda\sqrt{\mathcal{A}\Delta f}}{hc} \times \frac{\mathrm{EQE}}{i_{\mathrm{noise}}}, \quad (1)$$

[1]Sustainable Advanced Materials (Sêr-SAM), Department of Physics, Swansea University, Swansea, UK. [2]Institute for Materials Research (IMO), Hasselt University, Diepenbeek, Belgium. [3]IMEC, Associated Lab IMOMEC, Diepenbeek, Belgium. ✉e-mail: o.j.sandberg@swansea.ac.uk; ardalan.armin@swansea.ac.uk

where i_{noise} is the noise current, q the elementary charge, h is the Planck constant, c the speed of light, $\mathcal{A}$ the device area, Δf the frequency bandwidth, and EQE is the photovoltaic external quantum efficiency. Although the operational spectral window of OPDs has been expanded from the visible range up to $\lambda = 1{,}700$ nm, the highest D^* values above 1,500 nm have only reached modest levels of 10^9 cm Hz$^{1/2}$ W^{-1} (refs. [9,10]). The longer λ range has remained unattainable[11], despite the implementation of optical and electrical amplification[12], which can boost the EQE to as high as 2,000% (ref. [13]). The main obstacle for achieving higher D^* has proven to be the large dark current density J_D or, more precisely, the electrical shot noise produced by it (equation (1)) at the operational bias voltage V (typically −0.5 to −2 V).

In general, the dark current of an OPD operating in reverse bias is composed of two distinctly different components: a device-intrinsic diode component, represented by the dark saturation current density J_0, and an ohmic leakage current component (J_{shunt}). J_{shunt} is believed to originate from imperfections related to device fabrication and non-optimized device layouts that induce alternative conducting pathways, so called shunts (for example, pinholes in the active layer and lateral currents[14]). Conversely, J_0 is an inherent device parameter, determined by thermally activated radiative and non-radiative (NR) processes in the active layer and/or at the contacts, and being of the form $J_0 \propto \exp(-E_a/kT)$, where E_a is the associated activation energy of the dominant process and kT is the thermal energy. As such, the specific detectivity of OPDs is fundamentally limited by J_0, being the dominant source of noise for narrow-gap systems in particular. In BHJs, J_0 has been found to be dominated by non-radiative processes, resulting in J_0 levels substantially above those expected from radiative transitions alone[15]. However, the origin of the large non-radiative current, limiting the detectivities in OPDs, is currently hotly debated.

Three different mechanisms that contribute to J_0 in reverse bias have been suggested: (1) NR transitions via charge transfer (CT) states[16], (2) charge injection of (minority) carriers at the contacts[15] and (3) trap-mediated transitions[17,18]. These processes, however, are expected to display distinctly different E_a. For transitions taking place between the ground state and the CT states, we generally expect $E_a = E_{CT}$, where E_{CT} is the CT state energy, reflecting the effective D–A energy gap in BHJs. It has been shown that NR transitions via CT states limit the open-circuit voltage (V_{OC}) in organic solar cells, and thus are also expected to play a role in OPDs[19,20]. For minority carrier injection, in turn, J_0 is limited by the associated injection barrier at the electrode[21]. This barrier is effectively lowered by both energetic disorder and image-charge effects, resulting in a Poole–Frenkel-like current with a voltage-dependent E_a (refs. [22,23]). Although this process is important in the case of misaligned energy levels at the electrodes, it is commonly negligible for optimized ohmic contacts[21]. Finally, for trap-mediated transitions, E_a generally depends on the related trap energy and distribution; for mid-gap traps, $E_a = E_{CT}/2$ is typically expected. The presence of trap states has been suggested in a broad range of BHJ solar cells[24–29], but their shape and role in OPDs have remained elusive.

In this Article we provide evidence that the dark saturation current in OPDs is universally limited by transitions mediated by mid-gap states. From sensitive EQE measurements of a considerable number of D:A BHJ systems, the presence of radiative mid-gap states is observed. The active role of the mid-gap states in determining J_0 is further demonstrated by temperature-dependent measurements on narrow-gap BHJs, where the shunt effects are minimal, from which we find the E_a of J_D to be half the D–A energy gap. Additionally, the observed voltage dependence of J_D is consistently explained by mid-gap state-mediated transitions. Finally, the determined J_0 for the OPD systems considered in this work, along with a large set of literature-known narrow-gap systems, are observed to follow the general trend expected for mid-gap states. These results have several important implications for OPDs. First, a revised upper limit of D^* can be calculated. Second, the noise determined by mid-gap state-mediated currents displays different reverse-bias voltage characteristics and noise than expected for transitions mediated by CT states only. Third, these results highlight the importance of suppressing and identifying the origin of the mid-gap states, crucial to enhance the performance of OPDs. Finally, these findings are also highly pertinent for other photonic devices based on organic semiconductors, such as light-emitting diodes, solar cells and indoor photovoltaics.

Results and discussion

To clarify the dominant dark current mechanism in OPDs, we first quantify the radiative current components, which are generally dominated by energy-gap edge and sub-gap features in the EQE. To this end, we conducted ultra-sensitive EQE measurements on a wide range of D:A BHJ systems with different D–A energy gaps (Supplementary Fig. 1). Figure 1a presents the EQE spectra of three exemplary D:A systems, PBTQ(OD):$PC_{71}BM$, PBDB-T:$PC_{71}BM$ and PBDB-T:EH-IDTBR. The corresponding energy-level diagrams are depicted in Fig. 1b. The full names of the chemicals used are provided in the Methods. The EQE spectra, measured over a dynamic range of 90 dB, are shown on a logarithmic scale, illustrating the energy gap edges and the sub-gap spectral range.

The measured EQE spectra of the BHJs are generally found to display two distinct features in the sub-gap region: a CT state feature below the gap and an additional low-energy sub-gap feature, which is assigned to radiative transitions via mid-gap states. A schematic energy diagram with the respective radiative processes is shown in Fig. 1c. The CT state contribution is expected to follow a Gaussian function from which E_{CT} can be obtained. For narrow-gap BHJs, however, the E_{CT} is expected to be very close to the singlet exciton energy of the donor polymer, with the CT absorption shoulder correspondingly overshadowed by the donor singlet exciton absorption in these systems. As such, E_{CT} was instead estimated from the intercept between the measured EQE and the associated electroluminescence expected from detailed balance (see ref. [16] for details). We further note that the EQE tails directly below the gap approximately follow a $\ln(\mathrm{EQE}) \propto E/kT$ type behaviour[30], suggesting that exponential tail states, if present, will have a negligible impact.

Based on the measured EQE, the corresponding dark current density induced by radiative transitions (J_{RAD}) can be estimated[31]. In general, J_{RAD} can be written as a sum of the CT state contribution and the trap state contribution. In forward bias, at voltages comparable to the open-circuit voltage of solar cells, J_{RAD} in BHJs has been observed to be dominated by the CT state recombination[19]. In reverse bias, at voltages relevant for OPDs, however, the contribution from trap states is expected to play a decisive role. In accordance with detailed balance, the radiative current at small reverse bias is given by $J_{RAD} = qf_0^{\infty}\mathrm{EQE}(E)\,\phi_{BB}(E)\,dE$, where $\phi_{BB}(E)$ is the blackbody spectrum (E is the photon energy)[17]. Figure 1d shows the estimated J_{RAD} (at small reverse bias) as a function of E_{CT} for the BHJ systems considered (Supplementary Table 1). In (low offset) systems where CT states cannot be distinguished from singlet excitons, we used the optical gap as a proxy for E_{CT} instead. For comparison, we include the radiative J_0 (based on measured EQE) of six inorganic photodiodes with different bandgaps (E_g), showing an activation energy of $E_a = E_g$, consistent with band-to-band transitions dominating the radiative current in these systems. Conversely, for organic BHJs, J_{RAD} is found to scale with $E_a = E_{CT}/2$. This can be traced back to the dominant contribution from the low-energy EQE features (Fig. 1a), reflecting their Gaussian distributions characterized by energy gaps around $E_{CT}/2$, as expected for mid-gap states. These observations imply that J_{RAD} in BHJs is dominated by radiative transitions via mid-gap states at voltages relevant for OPDs.

To clarify the origin of the dominant NR process, we next conducted T-dependent J_D–V measurements on three different

https://doi.org/10.1038/s41566-023-01173-5

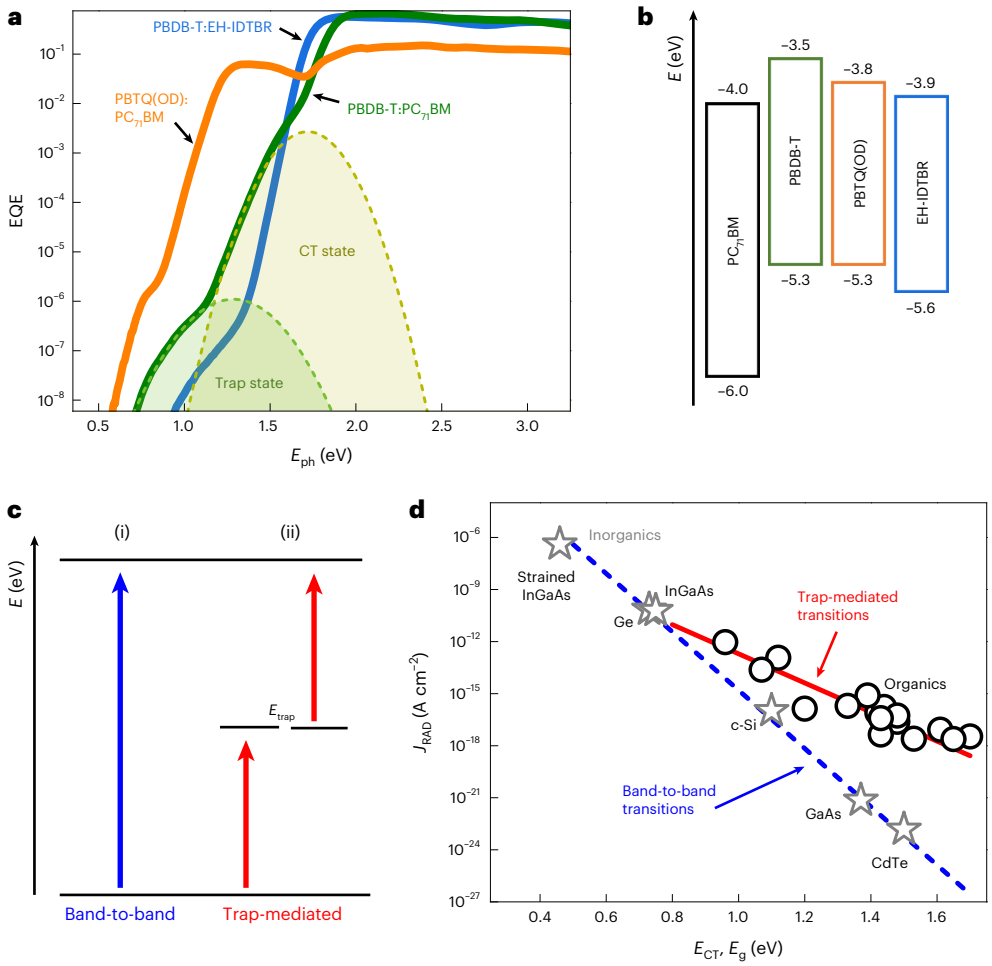

Fig. 1 | Sub-gap EQE features and the role of radiative trap states. a, Sensitive EQE spectra of the three different D:A BHJ blends with different D–A energy gaps. **b**, The corresponding highest occupied molecular orbital and lowest unoccupied molecular orbital energy levels. **c**, Schematic energy diagram showing the radiative transitions associated with (i) band-to-band or CT-mediated and (ii) trap-mediated transitions, underpinning the EQE features. **d**, The expected reverse-bias radiative current density (calculated from the EQE) for BHJ photodiodes with different D–A energies and compared to six commercial inorganic photodiodes. The trends expected for band-to-band ($E_a = E_g$) and mid-gap state-mediated transitions ($E_a = E_{CT}/2$) are indicated by the blue dashed line and red solid line, respectively.

narrow-gap D:$PC_{71}BM$ systems with PBTQ(OD), PTTBAI or PTTQ(HD) as the donor. The advantage of using narrow-gap BHJs is that the measured J_D directly reflects the J_0 of these devices, owing to their high J_0 (relative to the shunt). In Fig. 2a, the corresponding J_D measured at −0.1 V at room temperature (r.t.) is compared to the respective J_{RAD}. A voltage of −0.1 V was chosen to further minimize the effects of shunts (present at high reverse bias) and noise (at voltages near zero). We find that J_{RAD} is about six orders of magnitude below the experimental J_D (at low reverse bias), suggesting that J_0 is strongly dominated by NR transitions.

Figure 2b shows $J_D(-0.1\,V)$ as a function of $1/kT$ for the different narrow-gap blends. We find that $\ln|J_D|$ depends linearly on $1/kT$ for temperatures above 260 K. For temperatures below 260 K, deviations from linearity are seen, caused by the inability to measure currents below 10^{-12} A or the dominance of other current channels with weaker temperature dependences. Figure 2c shows the obtained E_a as a function of the D–A energy-level gap E_g (obtained from cyclic voltammetry[32,33]) and the estimated E_{CT}. Similar values are obtained for reverse bias voltages up to −1 V (Supplementary Fig. 2), suggesting that the contribution from shunts remains minimal at these voltages. Despite the uncertainties[34,35] of the energy gap, we generally observe $E_a \approx E_{CT}/2$ for the three narrow-gap BHJs. This is compared with the results from T-dependent measurements of three commercial NIR photodetectors composed of germanium (Ge) and strained and unstrained indium gallium arsenide (InGaAs) in Fig. 2c, where E_a equals the bandgap energy, as expected (Supplementary Figs. 3 and 4).

The observation that E_a is insensitive to the reverse-bias voltage and equals half of the related D–A gap energy suggests that J_D in narrow-gap OPDs are limited by mid-gap states. To substantiate this, we further clarified the corresponding voltage dependence of J_D. In general, the diode current component of J_D can be expressed as (Supplementary Note 1)

$$J_{\mathrm{diode},m}(V) = J_{0,m}\eta_{0,m}(V)\left[\exp\left(\frac{qV}{mkT}\right) - 1\right], \quad (2)$$

where m is the diode ideality factor, $J_{0,m}$ is the corresponding dark saturation current density, and $\eta_{0,m}(V)$ is a voltage-dependent prefactor accounting for the effect of nonuniform generation and recombination rates inside the active layer. For direct transitions $m = 1$, and $\eta_{0,1} = 1$ is typically expected. For trap-mediated transitions, generally described by Shockley–Read–Hall (SRH) statistics, however, m typically ranges between 1 and 2 depending on the energetic distribution of traps involved. In the case of mid-gap trap states[36] $m = 2$,

https://doi.org/10.1038/s41566-023-01173-5

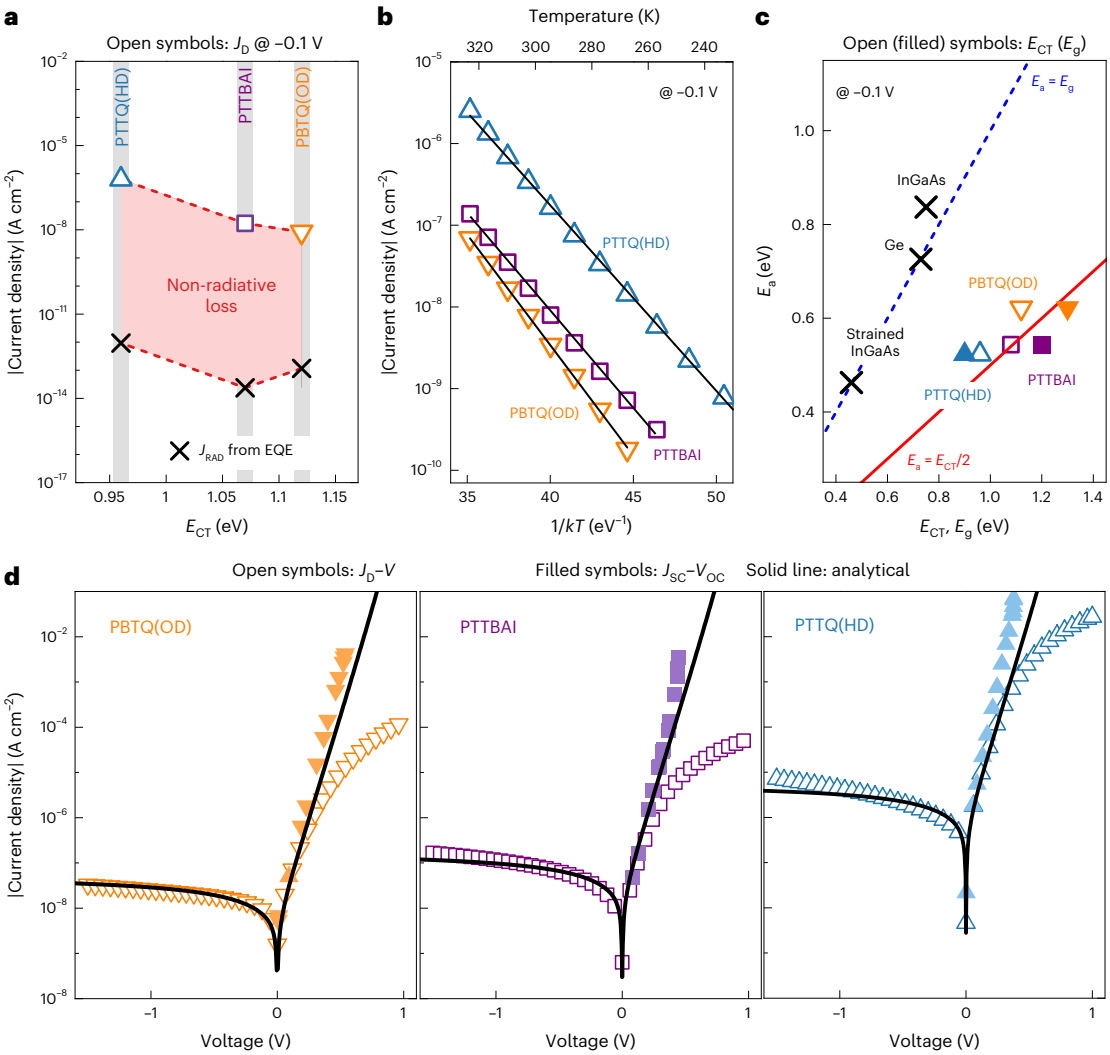

Fig. 2 | Temperature-dependent current measurements and dark current–voltage characteristics of narrow-gap OPDs. a, Measured $J_D(-0.1\,V)$ at r.t., and calculated radiative reverse-bias dark current density J_{RAD} as a function of E_{CT} for narrow-gap organic D:$PC_{71}BM$ blends. **b**,**c**, Corresponding $J_D(-0.1\,V)$ as a function of $1/kT$ (**b**) and the corresponding extracted activation energies E_a as a function of E_{CT} (**c**; open symbols) for narrow-gap organic D:$PC_{71}BM$ blends. The same BHJ data but shown as a function of D–A gap expected from cyclic voltammetry is indicated by filled symbols. Results from three commercial NIR inorganic photodiodes at different bandgaps E_g are included for comparison. **d**, Experimental J_D–V curves and J_{SC}–V_{OC} measurements of narrow-gap D:$PC_{71}BM$ photodiodes (symbols). The fits to equation (2) with $m = 2$ are indicated by solid lines.

with $\eta_{0,2}(V)$ exhibiting a sublinear but non-negligible V-dependence in the reverse bias (Supplementary Note 2).

The experimental J_D–V characteristics of the narrow-gap OPDs are shown in Fig. 2d and compared to the analytical model (equation (2)) with $m = 2$. At small forward bias and reverse bias, a good agreement is obtained between the experiments (symbols) and the analytical model with $m = 2$ (solid lines), using the associated J_0 as the only fitting parameter. We note that deviations between analytical and experimental currents at high reverse bias are eventually expected as the contribution of J_{shunt} increases. To validate that the dark current in the relevant forward-bias voltage regime is not limited by poor charge transport (for example, caused by low mobilities), we also included corresponding intensity-dependent short-circuit current density (J_{SC}) versus V_{OC} measurements, which are known to not be affected by limitations related to transport and series resistance[37]. These results corroborate the assertion that J_0 is dominated by thermal transitions via mid-gap trap states, simultaneously explaining the experimentally observed V-dependence of J_D in reverse and forward bias.

To assess the generality of these findings, we plot in Fig. 3a measured $J_D(-0.1\,V)$ for literature-known fullerene-based BHJs with $E_{CT} < 1.2$ eV (ref. [16]), alongside the BHJs investigated in this work (symbols). Indeed, for narrow-gap BHJ systems, the measured experimental $J_D(-0.1\,V)$ follow a general trend of $E_a = E_{CT}/2$ (solid lines), suggesting that $J_D(-0.1\,V)$ is limited by mid-gap-mediated transitions. Thus, the J_0 in these systems can be estimated from $J_D(-0.1\,V)$, based on equation (2) for $m = 2$ (at $V = -0.1\,V$), through $J_0 \approx J_D(-0.1\,V) \times (7.36\,(E_{CT}/eV) + 0.736)$; the corresponding J_0 are shown in Fig. 3b. The presence and dominant role of mid-gap states in narrow-gap BHJ systems in general is further corroborated by corresponding J_{SC}–V_{OC} data at 1 sun (Supplementary Fig. 5).

As J_0 decreases exponentially with increasing E_{CT}, however, $J_D(-0.1\,V)$ for BHJs with wider D–A gaps in Fig. 3a inevitably becomes dominated by J_{shunt}, overshadowing the true J_0. Although J_{shunt} dominates in the reverse bias of these systems, the diode current eventually becomes prevalent in the forward bias. This is demonstrated in the inset of Fig. 3a for PBDB-T:EH-IDTBR, showcasing the superposition between the symmetric shunt current density, typically of

https://doi.org/10.1038/s41566-023-01173-5

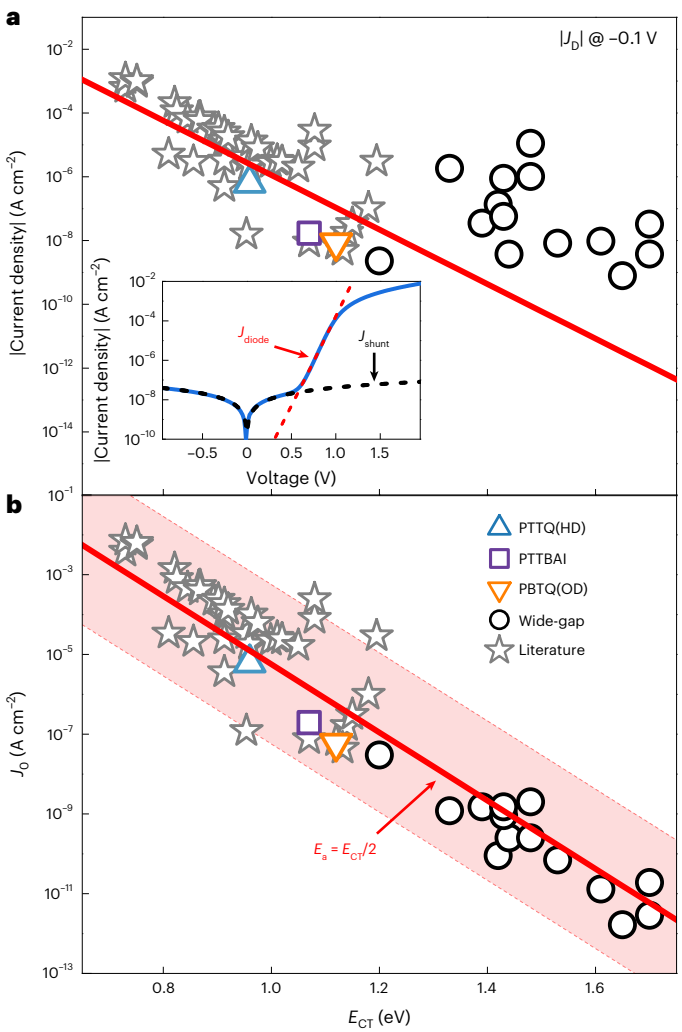

Fig. 3 | General trend of the dark current densities of OPDs. a, Experimentally determined J_D measured at −0.1 V as a function of E_{CT} of the OPDs studied in this work (triangles, square and circles) and a large set of narrow-gap BHJ systems from the literature (stars[16]). The inset shows the J_D–V characteristics of PBDB-T:EH-IDTBR, demonstrating the superposition of shunt (linear) and diode current ($m = 2$) components as well as the dominance of shunt in the reverse bias of systems with wide D–A gaps ($E_{CT} > 1.2$ eV). **b**, Extracted dark saturation current density as a function of E_{CT} of the OPDs studied in this work (triangles, square and circles), as well as those derived from literature values with $E_{CT} < 1.2$ eV (stars). Red lines represent the expected trend, $J_0 = J_{00} \exp\left(-\frac{E_{CT}}{2kT}\right)$, when mid-gap trap-mediated transitions ($E_a = E_{CT}/2$) dominate the dark current. Here, the red solid line corresponds to a J_0 with prefactor $J_{00} = 2{,}000$ A cm^{-2}. For comparison, we have included a shaded area with an upper bound corresponding to $J_{00} = 2 \times 10^5$ A cm^{-2} and lower bound corresponding to $J_{00} = 20$ A cm^{-2}.

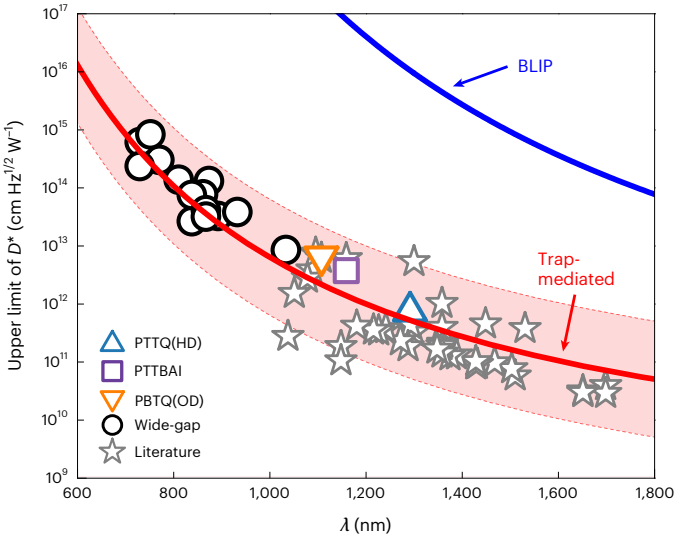

Fig. 4 | Upper limits of the specific detectivity D^* in OPDs. The estimated upper limit of D^* assuming noise governed by i_{shot} generated by J_0 (from Fig. 3b) for the BHJs studied in this work (triangles, square and circles) and narrow-gap systems from the literature (stars). The red solid line corresponds to the expected trend of the upper limit of D^* when mid-gap transitions dominate, calculated based on the red solid line in Fig. 3b (the shaded area represents the corresponding shaded area in Fig. 3b). The blue line marks the BLIP limit.

the form $J_{shunt} = V/(R_{shunt}\mathcal{A})$ (R_{shunt} is the shunt resistance), and the exponential diode current density (J_{diode}) contribution. Subsequently, the dark current in the forward bias can be used to extract J_0 for systems with wider D–A gaps. Indeed, we generally find that the dark current density at small forward bias, above the J_{shunt} level, is well-approximated by equation (2) with $m = 2$ (Fig. 3a, inset and Supplementary Fig. 6). Figure 3b shows the corresponding J_0 obtained for the wider-gap BHJs considered in this work. These systems are seen to follow the same trend as the narrow-gap systems, strongly suggesting that J_0 in OPDs is universally and fundamentally limited by mid-gap state-mediated transitions.

Based on these findings, a universal efficiency limit for D^* of OPDs can be obtained. In accordance with equation (1), D^* is inversely proportional to the measured noise current i_{noise}. Given that photodetectors are generally operated under reverse bias, i_{noise} is typically approximated by its shot noise component i_{shot} (ref. [38]), where $i^2_{shot} = 2qS\Delta f$ of any Poisson-distributed current signal S (ref. [39]). An upper limit of D^* can then be experimentally estimated from $D^* = q\lambda\left(hc\sqrt{2q|J_0|}\right)^{-1}$, assuming EQE = 1 with onset at $E = E_{CT}$. Figure 4 shows the estimated upper limits of D^*, based on the extracted J_0 for the BHJs from Fig. 3b. The corresponding trend expected for transitions mediated by mid-gap trap states is indicated by the red line, reproducing the general behaviour of the experimentally estimated upper limits of D^*. For comparison, the blue solid line in Fig. 4 indicates the background-limited infrared photodetector (BLIP) limit, corresponding to the upper theoretical limit of a perfectly radiative photodiode (that is, $J_D = J_{RAD}$, with EQE = 1 for $E \geq E_{CT}$ and EQE = 0 otherwise).

When calculating the expected noise current or analysing experimental noise measurements, it is important to emphasize that i^2_{noise}, and hence D^*, generally also depends on the applied voltage. As discussed in Supplementary Note 3, the voltage dependence of i^2_{noise} in reverse bias depends on the dominant current channel. If J_D is dominated by band-to-band transitions, a voltage-independent i^2_{noise} is expected for $V \ll -kT/q$ in the dark. On the other hand, if the dark current is dominated by transitions via mid-gap states, with J_D given by equation (2) in reverse bias, a sub-linear voltage dependence of i^2_{noise} is expected.

Finally, we emphasize that an understanding of the exact nature of the mid-gap trap states in OPDs has remained elusive. The trap states may have different origins and broad energetic distributions within the gap. However, as stipulated by SRH statistics[36], and further demonstrated experimentally in Supplementary Note 4, transitions mediated by trap states in the centre of the gap are most likely to occur. As a result, the J_0 in BHJ-based OPDs is also predominantly dominated by these mid-gap states. We note that these states are also observed in neat-material devices based on polymer, fullerene and non-fullerene small molecules, while being insensitive to the contacts used, suggesting an organic semiconductor material-

related origin (Supplementary Note 4). We speculate that the traps are probably caused by trace amounts of extrinsic impurities. To further substantiate this, and minimize trap-mediated contributions limiting OPD performance, future research should focus on the suppression and identification of the origin of mid-gap states.

Conclusion

To conclude, we have undertaken a detailed study on the origin of the dark saturation current in organic photodetectors based on next-generation organic semiconductors. Specifically, we have utilized temperature-dependent current measurements on narrow-gap organic semiconductor blend photodiodes to show that the thermal activation of the dark current at small reverse bias is consistent with mid-gap state-mediated transitions. Furthermore, we show that dark saturation current densities for a large set of OPDs universally follow a trend expected for transitions via mid-gap trap states. The presence of mid-gap states is further supported by sensitive EQE measurements. These results imply that J_0 in the reverse bias is fundamentally dominated by the mid-gap state-mediated transitions, setting an upper limit of D^* for OPDs. Therefore, to enhance the performance of OPDs it is important to suppress and identify the origin of mid-gap states. These findings are highly relevant for other organic semiconductor-based photonic diode applications as well.

Online content

Any methods, additional references, Nature Portfolio reporting summaries, source data, extended data, supplementary information, acknowledgements, peer review information; details of author contributions and competing interests; and statements of data and code availability are available at https://doi.org/10.1038/s41566-023-01173-5.

References

1. García De Arquer, F. P., Armin, A., Meredith, P. & Sargent, E. H. Solution-processed semiconductors for next-generation photodetectors. *Nat. Rev. Mater.* **2**, 16100 (2017).
2. Guo, Z., Park, S., Yoon, J. & Shin, I. Recent progress in the development of near-infrared fluorescent probes for bioimaging applications. *Chem. Soc. Rev.* **43**, 16–29 (2014).
3. Clark, J. & Lanzani, G. Organic photonics for communications. *Nat. Photon.* **4**, 438–446 (2010).
4. Yoon, S., Sim, K. M. & Chung, D. S. Prospects of colour selective organic photodiodes. *J. Mater. Chem. C* **6**, 13084–13100 (2018).
5. Kwon, J. et al. Three-dimensional monolithic integration in flexible printed organic transistors. *Nat. Commun.* **10**, 54 (2019).
6. Park, K. S. et al. Heterogeneous monolithic integration of single-crystal organic materials. *Adv. Mater.* **29**, 1603285 (2017).
7. Jansen-van Vuuren, R. D., Armin, A., Pandey, A. K., Burn, P. L. & Meredith, P. Organic photodiodes: the future of full color detection and image sensing. *Adv. Mater.* **28**, 4766–4802 (2016).
8. Ren, H., Chen, J., Li, Y. & Tang, J. Recent progress in organic photodetectors and their applications. *Adv. Sci.* **8**, 2002418 (2021).
9. Kaiser, C. et al. Manipulating the charge transfer absorption for narrowband light detection in the near-infrared. *Chem. Mater.* **31**, 9325–9330 (2019).
10. Tang, Z. et al. Polymer:fullerene bimolecular crystals for near-infrared spectroscopic photodetectors. *Adv. Mater.* **29**, 1702184 (2017).
11. Li, Q., Guo, Y. & Liu, Y. Exploration of near-infrared organic photodetectors. *Chem. Mater.* **31**, 6359–6379 (2019).
12. Lan, Z. et al. Near-infrared and visible light dual-mode organic photodetectors. *Sci. Adv.* **6**, eaaw8065 (2020).
13. Wang, W. et al. Organic photodetectors with gain and broadband/narrowband response under top/bottom illumination conditions. *Adv. Opt. Mater.* **6**, 1800249 (2018).
14. Zheng, Y., Fischer, A., Sergeeva, N., Reineke, S. & Mannsfeld, S. C. B. Exploiting lateral current flow due to doped layers in semiconductor devices having crossbar electrodes. *Org. Electron.* **65**, 82–90 (2019).
15. Simone, G. et al. On the origin of dark current in organic photodiodes. *Adv. Opt. Mater.* **8**, 1901568 (2020).
16. Gielen, S. et al. Intrinsic detectivity limits of organic near-infrared photodetectors. *Adv. Mater.* **32**, 2003818 (2020).
17. Zarrabi, N. et al. Charge-generating mid-gap trap states define the thermodynamic limit of organic photovoltaic devices. *Nat. Commun.* **11**, 5567 (2020).
18. Kublitski, J. et al. Reverse dark current in organic photodetectors and the major role of traps as source of noise. *Nat. Commun.* **12**, 551 (2021).
19. Benduhn, J. et al. Intrinsic non-radiative voltage losses in fullerene-based organic solar cells. *Nat. Energy* **2**, 17053 (2017).
20. Azzouzi, M. et al. Nonradiative energy losses in bulk-heterojunction organic photovoltaics. *Phys. Rev. X* **8**, 31055 (2018).
21. Sandberg, O. J. & Armin, A. On the effect of surface recombination in thin film solar cells, light emitting diodes and photodetectors. *Synth. Met.* **254**, 114–121 (2019).
22. Coehoorn, R. & Bobbert, P. A. Effects of Gaussian disorder on charge carrier transport and recombination in organic semiconductors. *Phys. Status Solidi A Appl. Mater. Sci.* **209**, 2354–2377 (2012).
23. Emtage, P. R. & O'Dwyer, J. J. Richardson-Schottky effect in insulators. *Phys. Rev. Lett.* **16**, 356–358 (1966).
24. Kirchartz, T., Pieters, B. E., Kirkpatrick, J., Rau, U. & Nelson, J. Recombination via tail states in polythiophene:fullerene solar cells. *Phys. Rev. B* **83**, 115209 (2011).
25. Street, R. A. Localized state distribution and its effect on recombination in organic solar cells. *Phys. Rev. B Condens. Matter Mater. Phys.* **84**, 075208 (2011).
26. Rauh, D., Deibel, C. & Dyakonov, V. Charge density dependent nongeminate recombination in organic bulk heterojunction solar cells. *Adv. Funct. Mater.* **22**, 3371–3377 (2012).
27. Tress, W., Leo, K. & Riede, M. Dominating recombination mechanisms in organic solar cells based on ZnPc and C60. *Appl. Phys. Lett.* **102**, 163901 (2013).
28. Wu, J. et al. Tail state limited photocurrent collection of thick photoactive layers in organic solar cells. *Nat. Commun.* **10**, 5159 (2019).
29. Zeiske, S. et al. Direct observation of trap-assisted recombination in organic photovoltaic devices. *Nat. Commun.* **12**, 3603 (2021).
30. Kaiser, C. et al. A universal Urbach rule for disordered organic semiconductors. *Nat. Commun.* **12**, 3988 (2021).
31. Shockley, W. & Queisser, H. J. Detailed balance limit of efficiency of *p-n* junction solar cells. *J. Appl. Phys.* **32**, 510–519 (1961).
32. Verstraeten, F. et al. Near-infrared organic photodetectors based on bay-annulated indigo showing broadband absorption and high detectivities up to 1.1 µm. *J. Mater. Chem. C* **6**, 11645–11650 (2018).
33. Verstraeten, F. et al. Efficient and readily tuneable near-infrared photodetection up to 1,500 nm enabled by thiadiazoloquinoxaline-based push-pull type conjugated polymers. *J. Mater. Chem. C* **8**, 10098–10103 (2020).
34. Vandewal, K., Benduhn, J. & Nikolis, V. C. How to determine optical gaps and voltage losses in organic photovoltaic materials. *Sustain. Energy Fuels* **2**, 538–544 (2018).
35. Bredas, J. L. Mind the gap! *Mater. Horizons* **1**, 17–19 (2014).

36. Sah, C. T., Noyce, R. N. & Shockley, W. Carrier generation and recombination in *p-n* junctions and *p-n* junction characteristics. *Proc. IRE* **45**, 1228–1243 (1957).
37. Tvingstedt, K. & Deibel, C. Temperature dependence of ideality factors in organic solar cells and the relation to radiative efficiency. *Adv. Energy Mater.* **6**, 1502230 (2016).
38. Fang, Y., Armin, A., Meredith, P. & Huang, J. Accurate characterization of next-generation thin-film photodetectors. *Nat. Photon.* **13**, 1–4 (2019).
39. Sze, S. M. & Ng, K. K. *Physics of Semiconductor Devices* (Wiley, 1981).

Methods

Materials

PTTBAI is an alternating copolymer (P) of TT (thieno[3,2-*b*]thiophene) and BAI (7,14-bis(4-(2-octyldodecyl)thiophen-2-yl) diindolo[3,2,1-*de*:3′,2′,1′-*ij*][1,5]naphthyridine-6,13-dione). **PBTQ(OD)** is an alternating copolymer (P) of B (benzene) and TQ(OD) (6,7-bis (5-(2-octyldodecyl)thiophen-2-yl)-4,9-di(thiophen-2-yl)-[1,2,5] thiadiazolo[3,4-*g*]quinoxaline). **PTTQ(HD)** is an alternating copolymer (P) of T (thiophene) and TQ(HD) (6,7-bis(5-(2-hexyldecyl) thiophen-2-yl)-4,9-di(thiophen-2-yl)-[1,2,5]thiadiazolo[3,4-*g*] quinoxaline). **PEDOT:PSS** (poly(3,4-ethylenedioxythiophene) polystyrene sulfonate) was purchased from Heraeus. Zinc acetate dehydrate, **PCDTBT** (poly[*N*-9′-heptadecanyl-2,7-carbazole-*alt*-5,5-(4′,7′-di-2-thienyl-2′,1′,3′-benzothiadiazole)]), **PCPDTBT** (poly[2,6-(4,4-bis-(2-ethylhexyl)-4*H*-cyclopenta(2,1-*b*;3,4-*b*′)-dithiophene)-*alt*-4,7-(2,1,3-benzothiadiazole)]) and **PBTTT** (poly[2,5-bis(3-tetradecylthiophen-2-yl) thieno[3,2-b]thiophene]) were purchased from Sigma Aldrich. **$PC_{71}BM$** ([6,6]-phenyl-C_{71}-butyric acid methyl ester), PDINO (perylene diimide functionalized with amino *N*-oxide), **BTP-eC9** (2,2′-[[12,13-bis(2-butyloctyl)-12,13-dihydro-3,9-dinonylbisthieno[2′,3′:4′,5′]thieno[2′,3′:4,5]pyrrolo[3,2-e:2′,3′-g][2,1,3] benzothiadiazole-2,10-diyl]bis[methylidyne(5,6-chloro-3-oxo-1*H*-indene-2,1(3*H*)-diylidene)]]bis[propanedinitrile]), **O-IDTBR** ((5*Z*,5′*Z*)-5,5′-((7,7′-(4,4,9,9-tetraoctyl-4,9-dihydro-*s*-indaceno[1,2-*b*:5,6-*b*′] dithiophene-2,7-diyl)bis(benzo[*c*][1,2,5]thiadiazole-7,4-diyl)) bis(methanylylidene))bis(3-ethyl-2-thioxothiazolidin-4-one)) and **EH-IDTBR** (5,5′-[[4,4,9,9-tetrakis(2-ethylhexyl)-4,9-dihydro-*s*-indaceno[1,2-*b*:5,6-*b*′]dithiophene-2,7-diyl]bis(2,1,3-benzothiadiazole-7,4-diylmethylidyne)]bis[3-ethyl-2-thioxo-4-thiazolidinone]) were purchased from Solarmer (Beijing). **BQR** (benzodithiophene-quaterthiophene-rhodanine) was provided by D. J. Jones (University of Melbourne). **PM6** (poly[(2,6-(4,8-bis(5-(2-ethylhexyl-3-fluoro)thiophen-2-yl)-benzo[1,2-*b*:4,5-*b*′] dithiophene)-*alt*-(5,5-(1′,3′-di-2-thienyl-5′,7′-bis(2-ethylhexyl) benzo[1′,2′-*c*:4′,5′-*c*′]dithiophene-4,8-dione))]), **Y6** (2,2′-((2*Z*,2′*Z*)-((12,13-bis(2-ethylhexyl)-3,9-diundecyl-12,13-dihydro-[1,2,5] thiadiazolo[3,4-*e*]thieno[2′,3′:4′,5′]thieno[2′,3′:4,5]pyrrolo[3,2-*g*] thieno[2′,3′:4,5]thieno[3,2-*b*]indole-2,10-diyl)bis(methanylylidene)) bis(5,6-difluoro-3-oxo-2,3-dihydro-1*H*-indene-2,1-diylidene))dimalononitrile), **ITIC** (3,9-bis(2-methylene-(3-(1,1-dicyanomethylene)-indanone))-5,5,11,11-tetrakis(4-hexylphenyl)-dithieno[2,3-*d*:2′,3′-*d*′]-*s*-indaceno[1,2-*b*:5,6-*b*′]dithiophene), **PBDB-T** (poly[(2,6-(4,8-bis(5-(2-ethylhexyl)thiophen-2-yl)-benzo[1,2-*b*:4,5-*b*′]dithiophene))-*alt*-(5,5-(1′,3′-di-2-thienyl-5′,7′-bis(2-ethylhexyl) benzo[1′,2′-*c*:4′,5′-*c*′]dithiophene-4,8-dione))]) and **PTB7-Th** (poly[4,8-bis(5-(2-ethylhexyl)thiophen-2-yl)benzo[1,2-*b*;4,5-*b*′] dithiophene-2,6-diyl-*alt*-(4-(2-ethylhexyl)-3-fluorothieno[3,4-*b*] thiophene-)-2-carboxylate-2-6-diyl]) were purchased from Zhi-yan (Nanjing) Inc. **m-MTDATA** (4,4′,4′-tris[(3-methylphenyl)phenylamino]triphenylamine) was purchased from Ossila. **PNDIT-F3N-Br** (poly[[2,7-bis(2-ethylhexyl)-1,2,3,6,7,8-hexahydro-1,3,6,8-tetraoxobenzo[lmn][3,8]phenanthroline-4,9-diyl]-2,5-thiophenediyl[9,9-bis[3′((*N*,*N*-dimethyl)-*N*-ethylammonium)]-propyl]-9*H*-fluorene-2,7-diyl-2,5-thiophenediyl]) was purchased from 1-materials.

Device fabrication

Commercial patterned indium tin oxide (ITO)-coated glass substrates from Ossila were used for the devices. The substrates were cleaned in an Alconox (detergent) aqueous solution bath at 60 °C, followed by sequential sonication in deionized water, acetone and 2-propanol for 10 min each. The cleaned substrates were dried with nitrogen and then treated in UV-ozone cleaner (Ossila, L2002A2-UK).

Devices based on the narrow-gap donor polymers PTTBAI, PBTQ(OD) and PTTQ(HD) were prepared using an inverted architecture, ITO/ZnO/PEIE/active layer/MoO_3/Ag. ZnO interlayers were spin-coated from a solution of $Zn(OAc)_2{\cdot}2H_2O$ (0.239 g; Merck) and ethanolamine (0.121 g; Merck) in 2-methoxyethanol (4 ml; Merck). The ZnO layers were annealed at 300 °C for 10 min to obtain a layer thickness of ~30 nm. Polyethylenimine ethoxylated (PEIE) was spin-coated from a solution of PEIE (0.1 ml; Merck) in isopropanol (35 ml) and thermally annealed at 100 °C for 10 min.

The active layer was deposited from a solution of narrow-gap polymer and $PC_{71}BM$ in solvent with mass ratios of 1 to 3, respectively, and total concentrations of 64, 48 and 32 mg ml^{-1} for PTTBAI (in *o*-dichlorobenzene with 7 vol/vol% of 1,8-diiodooctane (DIO)), PBTQ(OD) (in *o*-dichlorobenzene with 3 vol/vol% of DIO) and PTTQ(HD) (in chloroform with 3 vol/vol% of DIO), respectively. The solution was stirred overnight at 60 °C to ensure complete dissolution, and spin-coated on top of PEIE. The devices were finalized by the evaporation of top electrodes of MoO_3 (10 nm) and Ag (100 nm).

For the PBTTT:$PC_{71}BM$ device, an inverted architecture of ITO/ZnO/active layer/MoO_3/Ag was used. PBTTT and $PC_{71}BM$ was mixed in a weight ratio of 1:4 and total concentration of 32 mg ml^{-1} and dissolved in chloroform:1,2-dichlorobenzene (6:4 volume ratio). The solution was stirred overnight, filtered through a 0.2-μm polytetrafluoroethylene filter in the cold, and spin-coated at 65 °C for 60 s. A spin speed of 1,000 r.p.m., resulting in a thickness of 200 nm, was used for the active-layer deposition.

For devices based on wider D–A gaps, either a conventional or an inverted device architecture was used.

BQR:$PC_{71}BM$, PM6:BTP-eC9, PM6:BTP:eC9:PTTQ(HT), PM6:PTTQ(HD) and BTP-eC9:PTTQ(HD), neat PM6 and neat BTP-eC9 devices were fabricated with a conventional device architecture using PEDOT:PSS as the hole transport layer.

PEDOT:PSS solution was first filtered through a 0.45-μm polyvinylidene fluoride filter, then spin-coated (6,000 r.p.m. for 30 s, resulting in a thickness of 30 nm) onto ITO substrates and annealed at 155 °C for 15 min.

For the BQR:$PC_{71}BM$ device, BQR and $PC_{71}BM$ were dissolved in toluene (24 mg ml^{-1} with the D:A ratio of 1:1) and stirred at 60 °C for 3 h, then BQR:$PC_{71}BM$ solution was spin-coated (1,000 r.p.m.) on the PEDOT:PSS layer to achieve a film thickness of 100 nm. The BQR:$PC_{71}BM$ films were further exposed to a tetrahydrofuran environment in a closed Petri dish for 20 s, then thermally annealed (90 °C) for 10 min. Layers of 20 nm of Ca and 100 nm of Al were evaporated as the top electrodes.

For the PM6:BTP-eC9 device, a conventional architecture (ITO/PEDOT:PSS/active layer/PNDIT-F3N-Br/Ag) was used. PM6:BTP-eC9 with a weight ratio of 1:1.2 and total concentration of 17 mg ml^{-1} was dissolved in a CF:DIO (volume ratio of 99.5:0.5) solution. A spin speed of 3,500 r.p.m. (resulting in a thickness of 100 nm) was used for the active-layer deposition. The active layer was then thermally annealed at 90 °C for 10 min, and 0.5 mg $ml^{-1}$of PNDIT-F3N-Br (dissolved in methanol) solution was spin-coated on the PM6:BTP-eC9 film at 5,000 r.p.m. to form a 10-nm electron-transport layer. For the PM6:BTP-eC9:1% PTTQ(HT), PTTQ(HD) with a concentration of 1% by weight of the total concentration of PM6 and BTP-eC9 was added to the active-layer solution. The device architecture and deposition procedure were similar to those for the PM6:BTP-eC9 device.

For the neat PM6, neat BTP-eC9, PM6:1% PTTQ(HD) and BTP-eC9:1% PTTQ(HD) devices, a conventional architecture of ITO/PEDOT:PSS/active layer/Ca/Ag was used. The active-layer solution was made in CF with concentrations of 16 mg ml^{-1}, 16 + 0.16 mg ml^{-1}, 20 mg ml^{-1} and 20 + 0.2 mg ml^{-1} for the neat PM6, PM6:PTTQ(HD), neat BTP-eC9 and BTP-eC9:PTTQ(HD), respectively. A spin speed of 1,000 r.p.m. was used for active-layer deposition. Layers of 20 nm of Ca and 100 nm of Ag were evaporated as the top electrodes.

For neat $PC_{71}BM$, 7 nm of MoO_3 was evaporated on an ITO substrate, then 40 mg ml^{-1} of $PC_{71}BM$ in CF was deposited on top of a MoO_3 layer via spin coating with a spin speed of 1,000 r.p.m. Layers of 20 nm of Ca and 100 nm of Ag were evaporated as the top electrodes.

The other devices were fabricated with an inverted device architecture: ITO/ZnO/active layer/MoO_3(7 nm)/Ag(100 nm).

PCDTBT:$PC_{71}BM$ and PCDTBT:$PC_{71}BM$:1% *m*-MTDATA devices were fabricated with an inverted architecture (ITO/ZnO/PCDTBT:$PC_{71}BM$:*m*-MTDATA/MoO_3/Ag). First, 30 mg of PCDTBT:$PC_{71}BM$ with a blend ratio of 1:4 (that is, 6 mg of PCDTBT and 24 mg of $PC_{71}BM$) was dissolved in 800 µl of chlorobenzene (CB; two batches), then 200 µl of a solution containing 0.06 mg and 0 mg of *m*-MTDATA (M_w = 789.02 g mol^{-1}) was added to the first solutions to obtain final solutions containing 1% and 0% by weight of *m*-MTDATA in PCDTBT. The solution was spin-coated using a spin speed of 800 r.p.m. to obtain an active-layer thickness of 90 nm.

PM6:O-IDTBR was dissolved in a CB solution (18 mg ml^{-1}) with a D:A ratio of 1:1, and spin-coated (1,000 r.p.m.) on ZnO to form a 100-nm film.

PBDB-T:EH-IDTBR was dissolved in a CB solution (14 mg ml^{-1}) with a D:A ratio of 1:1, and spin-coated (8,000 r.p.m.) on ZnO to form a 100-nm film, then 7 nm of MoO_3 and 100 nm of Ag were evaporated as the top electrodes.

PBDB-T:ITIC was dissolved in a CB solution (14 mg ml^{-1} with 0.5 vol% DIO) with a D:A ratio of 1:1, and spin-coated (8,000 r.p.m.) on ZnO to form a 100-nm film. The active layer was further treated with thermal annealing at 100 °C for 10 min.

PBDB-T:$PC_{71}BM$ was dissolved in a CB solution (14 mg ml^{-1} with 3 vol% DIO) with a D:A ratio of 1:1.4, and spin-coated (1,000 r.p.m.) on ZnO to form a 100-nm film. The as-cast films were subsequently rinsed with 80 µl of methanol at 4,000 r.p.m. for 20 s to remove the residual DIO. PCPDTBT:$PC_{71}BM$ was dissolved in a DCB solution (40 mg ml^{-1}) with a D:A ratio of 1:4, and spin-coated (1,500 r.p.m.) on ZnO to form an 80-nm film. PM6:ITIC was dissolved in a CB solution (18 mg ml^{-11} with 0.5 vol% DIO) with a D:A ratio of 1:1, and spin-coated (1,000 r.p.m.) on ZnO to form a 100-nm film. The active layers were further treated with thermal annealing at 100 °C for 10 min. PM6:Y6 was dissolved in a CF solution (14 mg ml^{-1} with 0.5 vol% CN) with a D:A ratio of 1:1.2, and spin-coated (3,000 r.p.m.) on ZnO to form a 100-nm film. The cast active layers were further treated with thermal annealing at 110 °C for 10 min.

PTB7-Th:ITIC was dissolved in a CB solution (14 mg ml^{-1} with 1 vol% DIO) with a D:A ratio of 1:1.4, and spin-coated (1,000 r.p.m.) on ZnO to form a 100-nm film.

PTB7-Th:$PC_{71}BM$ was dissolved in a CB solution (14 mg ml^{-1} with 3 vol% DIO) with a D:A ratio of 1:1.5, and spin-coated (600 r.p.m.) on ZnO to form a 100-nm film. The as-cast films were rinsed with 80 µl of methanol at 4,000 r.p.m. for 20 s to remove the residual DIO. All top electrodes were deposited by thermal evaporation under a vacuum of 10^{-6} torr with an appropriate mask (from Ossila) to define a 0.04-cm^2 cell area for each pixel.

EQE

For the EQE measurements, a homebuilt set-up was used that included a Perkin Elmer UV/Vis/NIR spectrophotometer (LAMBDA 950) as a source of monochromatic light[40]. The light was chopped at 273 Hz and directed onto the device under test (DUT). The resulting photocurrent was amplified by a low-noise current amplifier (FEMTO DLPCA-200) and measured with a Stanford SR860 lock-in amplifier. To decrease the noise floor of the set-up, the DUT was mounted in an electrically shielded Linkam sample holder (Linkam, LTS420E-P) and an integration time of 30 s on the lock-in amplifier was used for detecting wavelengths above 1,500 nm. NIST-calibrated Si and Ge photodiodes (Newport) were used as calibration references.

Dark current density–voltage and temperature-dependent current measurements

The J_D–V characteristics were measured with a Keithley 2450 source measure unit scanning from the reverse to forward bias regime. The DUT was mounted in a temperature-controlled and electromagnetically shielded sample stage (Linkam, LTS420E-P), which was connected to a temperature controller (Linkam, T96) and a liquid-nitrogen pump (Linkam, LNP96), allowing for the temperature to be changed. In addition, *T*-dependent current measurements were conducted, where the current was measured continuously under a constant applied bias for a given temperature. This ensures that trapped charge carriers have sufficient time to be released and reach the electrodes, while minimizing the impact of both the voltage-sweep direction and the input impedance of the source measure unit (especially at low current levels near to zero applied bias voltage) when determining the activation energy.

Short-circuit current density versus open-circuit voltage

A custom-built continuous-wave laser operating at 520 nm was used for J_{SC}–V_{OC} measurements. The incident light intensity was stepwise increased by a motorized two-wheel attenuator from Standa (10MCWA168-1) containing different optical density filters. A Keithley 2450 source measure unit was used to record J_{SC} and V_{OC} of the DUT at each incident light intensity.

Gaussian fits to the EQE

The expected EQEs and energy gaps (E_j) of CT states (j = CT) and trap states (j = trap) were obtained by fitting the associated sub-gap absorption features in the experimental EQE data with a Gaussian function of the form

$$g_j(E) = \frac{f_j}{E\sqrt{4\pi\tilde{\lambda}_j kT}} \exp\left(-\frac{\left(E_j + \tilde{\lambda}_j - E\right)^2}{4\tilde{\lambda}_j kT}\right),$$

in accordance with the Marcus theory. Here, $\tilde{\lambda}_j$ is the corresponding reorganization energy, and f_j is a prefactor reflecting the oscillator strength and magnitude of light absorption.

Data availability

The experimental data in the main figures are provided in a tabulated excel file format as Supplementary Data. Additional supporting data are available from the corresponding authors upon reasonable request.

Code availability

The drift-diffusion simulator used in this study has been described in detail elsewhere[29,41]. Further information is available from the corresponding authors upon reasonable request.

References

40. Zeiske, S., Kaiser, C., Meredith, P. & Armin, A. Sensitivity of sub-bandgap external quantum efficiency measurements of solar cells under electrical and light bias. *ACS Photonics* **7**, 256–264 (2019).
41. Sandberg, O. J., Nyman, M. & Österbacka, R. Effect of contacts in organic bulk heterojunction solar cells. *Phys. Rev. Appl.* **1**, 024003 (2014).

Acknowledgements

This work was funded through the Welsh Government's Sêr Cymru II Program 'Sustainable Advanced Materials' (Welsh European Funding Office—European Regional Development Fund). C.K. is recipient of a UKRI EPSRC Doctoral Training Program studentship. P.M. is a Sêr Cymru II Research Chair and A.A. is a Rising Star Fellow also funded through the Welsh Government's Sêr Cymru II 'Sustainable Advanced Materials' Program (European Regional Development Fund, Welsh European Funding Office and Swansea University Strategic Initiative). This work was also funded by UKRI through the EPSRC Programme

grant EP/T028513/1 Application Targeted Integrated Photovoltaics. S.G. acknowledges the Research Foundation–Flanders (FWO Vlaanderen) for granting him a PhD fellowship. K.V. and W.M. are grateful for project funding by the FWO (G0D0118N, G0B2718N and GOH3816NAUHL).

Author contributions

A.A. and P.M. provided the overall leadership of the project. O.J.S. and A.A. conceptualized the idea. O.J.S., C.K. and A.A. designed the experiments. O.J.S. developed the theoretical model and performed the simulations. C.K., S.Z. and N.Z. performed the measurements. C.K. and N.Z. fabricated the devices. S.G. assisted in the device fabrication and data analysis. W.M. provided the narrow-gap materials. O.J.S., C.K., A.A. and K.V. interpreted the data. All authors contributed to the development of the manuscript, which was initially drafted by C.K. and O.J.S.

Competing interests

The authors declare no competing interests.

Additional information

Supplementary information The online version contains supplementary material available at https://doi.org/10.1038/s41566-023-01173-5.

Correspondence and requests for materials should be addressed to Oskar J. Sandberg or Ardalan Armin.

Peer review information *Nature Photonics* thanks Elizabeth von Hauff, Adam Moule and the other, anonymous, reviewer(s) for their contribution to the peer review of this work.